Chemistry Africa
https://doi.org/10.1007/s42250-021-00299-9

ORIGINAL ARTICLE

A Ruthenium Bipyridyl Molecular Dye Sensitizer and an Excited-State Intermolecular Proton Transfer-Active Colorimetric Probe for Anions, with High Affinity Towards CN^- in DMSO

Johannes H. Naimhwaka[1] · **Likius Daniel**[1] · **Eunike N. Hamukwaya**[1] · **Paulina T. Endjala**[1] · **Ateeq Rahman**[1] · **Veikko Uahengo**[1]

Received: 5 June 2021 / Accepted: 17 November 2021

Abstract

A ruthenium bipyridyl-dye sensitizer (**N**) based on the naphthyl-thiazole anchoring-ancillary ligand was synthesized and characterized using spectroscopic methods of UV–Vis, ^{1}H NMR, FTIR and fluorescence. The functional properties of **N** were investigated through its photoinduced and intramolecular based charge transfer mechanisms. Subsequently, **N** displayed interesting charge transfer-based properties (ESIPT) that are complementary to molecular photovoltaic and chemosensing properties. The properties were investigated and studied in dimethyl sulfoxide (DMSO), due to its polar nature and solubility of the dye. Dye sensitizer exhibitions were investigated through solvatochromism effect on the optoelectronic properties, while chemosensing abilities were inspected through colorimetric activities, upon molar addition of anions. Thus, it was established that a dual functional **N** is a potential dye sensitizer with optoelectronic properties displaying high molar extinction coefficients in acetone. In addition, it was found that **N** is a colorimetric and fluorometric probe selective and sensitive to biologically important anions of CN^-, F^-, OH^- and AcO^- through fluorescence enhancement, as a result of hydrogen-bonding leading to deprotonation. The sensing probe, however, displayed more strongly association with CN^-.

Keywords Molecular photovoltaic · Ruthenium dye sensitizer · Colorimetric probe · Solvatochromism · CN^- sensor

1 Introduction

Dye-sensitized solar cells (DSSC), falling under third generation type of solar cells, are playing a major role in the field of solar materials, attributed to their low cost and compatibility with flexible substrates as well as cost effective manufacturing methods [1]. Other advantages on board includes, energetic and structural tenability, environmental friendliness and chemical versatility, and facile synthetic approach to molecular structures. In addition, DSSCs can perform very well under diffused light conditions [2] and moderate temperature up to 50 °C and the theoretical PCE of the cell is estimated to be 32%, however, so far the highest efficiency recorded over the last 26 years is 13% [3–5].

The dye sensitizer can either be organic, natural (obtained from flowers, leaves and fruits) or inorganic in nature [6–8]. Inorganic metal complex dyes generally can consist of a metal centre, particularly a ruthenium (Ru (II)) metal, coordinated to smartly resonate anchoring ligands. The ruthenium-dye complex must inhibit panchromatic ability (broad light absorption range from the blue to the red region), with a high molecular stability to meet potential applications as a dye sensitizer [9–11]. The primary function of the ruthenium dye is to generate electrons upon absorption of/or exposure to visible light. In addition, these inorganic-based dyes have a compatible electronic energy to that of a visible-light powered photons (1.72 eV), normally characterized spectrally by a metal–ligand charge transfer (MLCT) absorption broad band, a channel for electrons into TiO_2 [12]. Even though ruthenium-based sensitizers have their own demerits such as high cost, limited availability of the starting materials and their toxicity; the advantages largely offsets their relatively lower efficiency comparing to their polycrystalline silicon cells [13, 14].

✉ Veikko Uahengo
vuahengo@unam.na; vuahengo@gmail.com

[1] Department of Chemistry and Biochemistry, University of Namibia, 340 Mandume Ndemufayo Avenue, Windhoek 9000, Namibia

Scheme 1 Molecular structures of, **a 1** and **b N**, the Ruthenium (II) bipyridyl complex dye

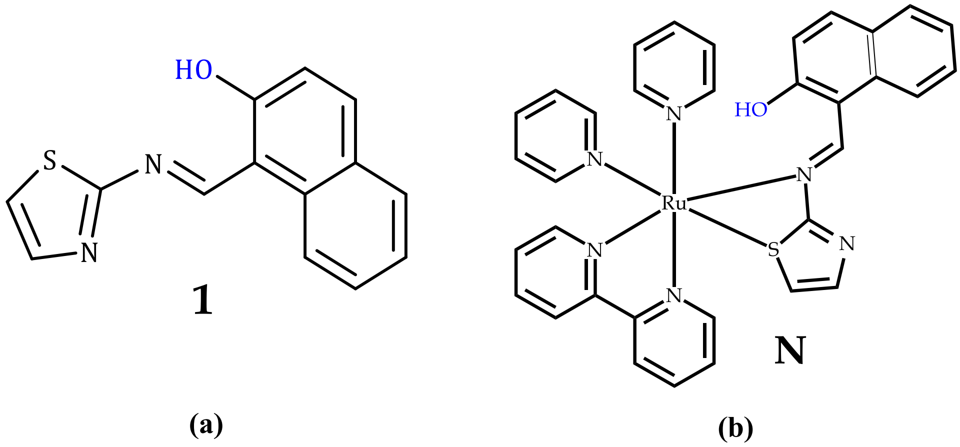

Furthermore, due to their structural make-up, electronic properties and excellent charge transfer mechanisms; ruthenium-dye sensitizers may be utilized as artificial receptors for the detection of specific ion in organic aqueous environments; a process known as chemosensing [15, 16]. The phenomenon of chemosensing is based on the discrimination of analyte species, a process triggered by the chemical association of guest and host molecules, leading to a guest–host complex formed, normally measurable through changes such as fluorescence and/or colour changes [17–19]. The process of chemosensing is a necessity in technologically advancing systems, because of the need to monitor ionic species in different mediums, due to their important roles in biological, environmental, clinical and chemical applications [20–23]. Moreover, metal complex-based chemosensors displayed a huge advantage over their organic counterparts, due to the high potential of dissolving in aqueous environments, which is a pre-condition of an ideal sensor in real samples, as most target analytes are found in aqueous mediums, both in physiological or environmental environments [22, 24].

Colorimetric probes for cations or anions have equally gained ascendancy over the last 20 years, due to their nature of application and performance being highly practical, due to their ability to produce a signal in the form of virtual colour changes, detectable by naked eye, upon binding with analytes in solution [25]. Hence, the development of chemosensors has enabled the establishment of a quick and simple method of detecting and controlling the levels of inorganic anions with hazardous abilities in natural environments [19]. Significantly, among other anions, cyanide ion (CN^-) as an extremely toxic inorganic anion is harmful to the environment and human health. However, its wide range of industrial applications, particularly in gold mining, electroplating, and various chemical industries, leads to unavoidable environmental spills. It is inevitable that some cyanide ion will leak into water streams along with industrial waste-water. The maximum concentration of cyanide in drinking water permitted by the world health organization is 1.9 µM. Due to the indispensability of cyanide in industrial production, it is necessary to use a simple and intuitive method to selectively and sensitively detect the cyanide content [26–29].

Furthermore, the photophysical properties of excited state intramolecular proton transfer (ESIPT) processes in fluorescence spectroscopy have generated considerable interest for both fundamental investigations and applications of organic molecules. However, most ESIPT chromophores are limited to hydroxyphenyl derivatives, and very few ESIPT chromophores have been reported to date. Herein, we have designed a ruthenium bipyridyl dye sensitizer (**N**) based on a naphthyl-thiazole anchoring ligand [30], with good photon absorption characteristics and capable of colorimetrically detect biologically important anions, such as cyanide (CN^-), Fluoride (F^-), Acetate (AcO^-) and hydroxide (OH^-) in dimethyl sulfoxide (DMSO). Moreover, the fact that **N** contains a naphthyl-thiazole group (**1**) bearing a hydroxyl group, which has been investigated for both chemosensing and photovoltaic properties in our previous study [31]. Thus, it is logically expected for **N** to exhibit anion-binding capability, where the acidities of the OH protons are drastically enhanced upon the photoexcitation, and therefore an excited-state intermolecular proton transfer (ESIPT) channel might be opened [32–34]. Furthermore, a photoactive ruthenium bipyridyl moiety can not only enhance the affinity through electrostatic interactions, but also provide a PET and ESIPT chromogenic/fluorogenic signalling channel [35–38]. The molecular structure of **1** and **N** are shown accordingly (Scheme 1).

2 Experimental

2.1 General

All reagents used were of analytical grade, used as received from the commercial sources, unless mentioned. UV–Vis spectroscopy was performed with Perkin Elmer Lambda

35 spectrophotometer in a standard 3.0 ml quartz cuvette with 1 cm path length. FT-IR spectra were obtained on a Perkin Elmer Spectrum 100 FTIR spectrometer. ^{1}H NMR spectra were recorded on a Varian Mercury VX-300 MHz spectrometer in $CDCl_3$, steady state excitation and emission spectra were obtained on the Molecular Device spectarMax M2. Elemental analyses (C, H and N) were carried out on a Perkin Elmer 240C analytical instrument. The density functional theory (DFT) calculations at B3LYP/6-31G** were performed using a Spartan'14 package software. All the measurements were carried out at ambient temperature.

2.2 Solvatochromic Measurements

The solution of **N** (1×10^{-5} M) was prepared in different solvents, such as Ethanol (EtOH), Methanol (MeOH), Acetone, Tetrahydrofuran (THF), Dimethyl Sulfoxide (DMSO) and Ethyl Acetate (EtAOc). The UV–Vis absorption spectra were analyzed using a Lambda 35 spectrophotometer.

2.3 Synthesis Procedures

2.3.1 Synthesis of N

The dye (**N**) was synthesized according to a known procedure [39]. A solid $AgNO_3$ (0.2731 g; 0.854 mmol) was added to $Ru(bpy)_2Cl_2.2H_2O$ [1.7141 g; 4.72 mmol] in 60 ml of ethanol. The mixture was refluxed for 1 h. After cooling, the AgCl precipitation was filtered out, washed with ethanol. To the filtrate, ligand **1** [31] was added (1.090 g; 0.00472 mol) and refluxed for 8 h. The solution was allowed to cool to room temperature and filtered (solid discarded), then most of the solvent (from the filtrate) was evaporated to dryness 90%. To the cooled residue, $NaClO_4.H_2O$ in ethanol (200 ml concentrated) was added, then followed by ice cold distilled water. Brown precipitate appeared (**N**) and filtered out and repeatedly washed with cold water [40]. Yield 60%. Elemental Analysis calcd (%) for $C_{35}H_{29}N_5ORuS$: C 62.86, H 4.37, N 10.47, O 2.39, Ru 15.11, S 12.61 Found: C 64.21, H 2.53, N 8.78, O 4.22, N 11.12. UV–vis (λ 455 nm, ε 1.6×10^4 L mol^{-1} cm^{-1}) and FTIR (OH 2889–3036 cm^{-1}; C–H, C=C, C=N 500–1750 cm^{-1}) (Scheme 2).

3 Results and Discussions

3.1 Photovoltaic Properties

3.1.1 Photophysical Property Studies of N

The UV–vis spectra of **N** and the corresponding ligand (**1**) are displayed respectively (Fig. 1). The metal complex dye (**N**) is defined by two intense peaks in the ultraviolet region (317 nm and 354 nm) and another broader band in the visible region of the spectrum (425–625 nm). Normally, absorption bands in the UV-region are ascribed to the overlapped π–π* intra ligand transitions (ILCT) of the ligands, while the broad absorption band in the visible region (425–625 nm) are attributable to the metal to ligand charge transfer (MLTC) transitions of the of metal complexes. The

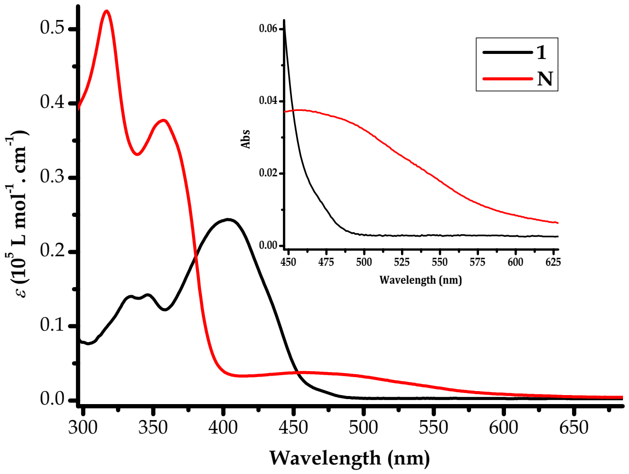

Fig. 1 Absorption spectra of **N** and **1**, both (1×10^{-5} M) in DMSO

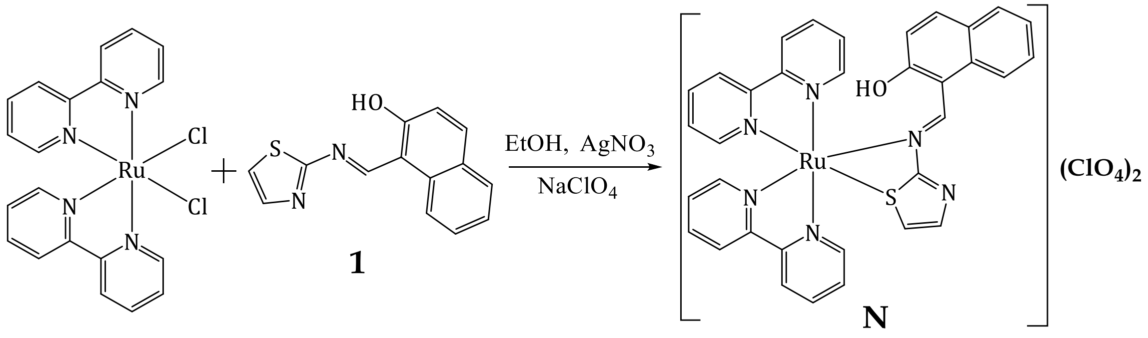

Scheme 2 Synthetic route of **N**

spectral characteristics for of **1** were extensively discussed in our previous work (32). Moreover, the extended absorption bands into the visible light region (≥ 400 nm) of **1,** which are ascribed to photoinduced charge transfers is an indication that it can function as a molecular photovoltaic material for solar cells. Moreover, **N** displays a broad band over a wide functional range due to the MLCT and which is expected to have better photocatalytic properties compared to **1**, which bears a high molar extinction coefficient.

3.1.2 Solvatochromic Studies of N

In theory, solvents have strong influence on the excited state of donor–acceptor compounds by stabilizing the molecules through hydrogen bonding, dipole–dipole, and solvation interactions. Thus, the spectral behaviours of **N** in different solvents were investigated to establish the effect of solvent polarities on absorption properties (Fig. 2). It was evident, the dye could only experience a slight red-shift in THF solvent, while in all other solvents used, the only effect was associated with the molar extinction coefficient (ε), which was high to low, for acetone to ethyl acetate (Fig. 2). In ruthenium dyes, the overall efficiency of the cell depends on two factors, the broader absorption functional range as well as the molar absorptivity. The broader the absorption range which can be extended to NIR (near infrared) region, the better the overall efficiency of the cell. Another parameter which increases the overall efficiency when it is high, is the molar extinction coefficient (ε) of the dye. Thus, the combination of high extinction coefficient (ε) and the broader absorption range of the dye, as in the case of **N**, signifies a potential photovoltaic material for solar cells. Thus, the variation of spectral in different solvents validates the fact that solvent polarities have a major impact on the absorption properties of the dye among other parameters.

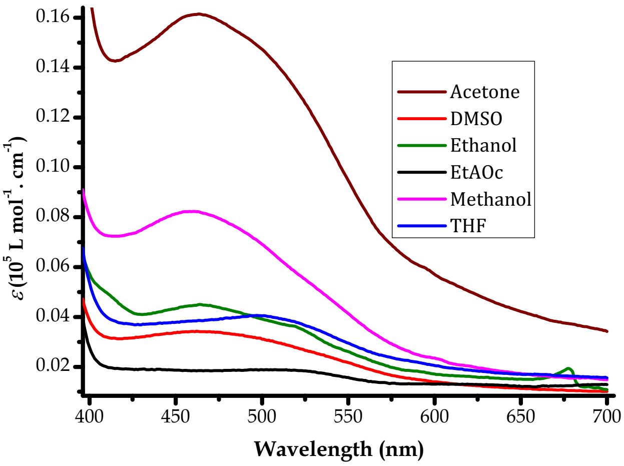

Fig. 2 Absorption spectra of **N** (1×10^{-5} M) in different solvents, for solvatochromism studies

3.1.3 The Optoelectronic Studies of N

The optoelectronic properties of **N** were investigated in different solvents of varying polarities (Fig. 2). Apart from observing the absorption properties of **N**, another fundamental parameter used to measure the potency of a good photovoltaic material is the energy gap (HOMO–LUMO gap). The magnitude or size of the field splitting between the HOMO and the LUMO needs to be compatible to the energy carried by photons within the visible light spectrum. The HOMO–LUMO energy gap which qualifies a molecular system to be classified as a solar harvesting material should fall within the wavelength range of ≥ 400 nm (≤ 3 eV) towards NIR. The ruthenium bipyridyl derivatives are known to absorb photons within the visible light region, hence the MLCT band in this region, with the energy gap ranging from 2 to 0.6 eV [8], which is well within the ≤ 3 eV for visible light spectrum. Thus, with introduction of **1**, a potential photon harvester itself, there is a good chance that the sum of the two parts results in a great photovoltaic performance. In Table 1, **N** has displayed varying absorption ranges at different maxima, which obviously translates into different HOMO–LUMO gaps, which are all displaying optical responsiveness within the visible light region, thus qualifying as a dye sensitizer. Several methods are used to determine the band gaps of molecular dyes, experimentally and theoretically.

The absorption spectra are key determinants to deducing the optoelectronic properties of molecular dye systems. The HOMO–LUMO gap of a molecular system can be determined by performing the extrapolation on the absorption spectrum of a compound, in order to determine the energy gap range (Fig. 3). The information of how a band gap or HOMO–LUMO gap can be calculated is shown, in Acetone and DMSO, obtained from the first optical absorption edges, and use the equation (Eq. 1) below to estimate E_g or $E_{H\text{-}L}$.

Table 1 UV–visible absorption parameters of **N** and the band gaps in different solvents

Solvent	λ_{max} (nm)	ε (10^4 L mol^{-1} cm^{-1})	λ_{onset} (nm)	$E_{H\text{-}L}$ (eV) (band gap)
Ethanol	464	0.45	600	2.07
Methanol	460	0.83	607	2.04
THF	501	0.41	615	2.02
Acetone	463	1.62	619	2.00
Ethyl Acetate	504	0.21	600	2.07
Dimethyl Sulfoxide	462	0.35	610	2.03

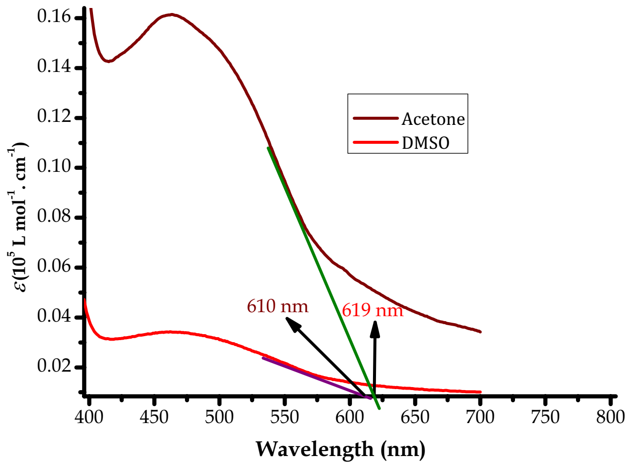

Fig. 3 Absorption spectrum and optical onset band gap of **N** (in Acetone and DMSO)

$$E_{H-L}(\text{eV}) = 1240/\lambda(\text{nm}) \qquad (1)$$

E_g ($E_{H\text{-}L}$) is the band gap (orbital energy gap) corresponding usually to a particular absorption of low photon energy ($h\nu$) and express the radiation energy in eV, while h is Planck constant and c is speed of light in vacuum. The summary of all the optical absorption spectra of **N** in all the solvents were calculated and compared, with results displayed in Table 1. The absorption spectrum of **N** in acetone is not only showing the highest molar absorptivity coefficient (1.6×10^4 L mol^{-1} cm^{-1}), but prominently also a wide absorption range (from 400 to over 700 nm), corresponding to the HOMO–LUMO gap of 1.71 eV. Generally, this translates into the dye system that fits the characteristics of an ideal dye sensitizer, for solar cells. Moreover, the optoelectronic properties of **N** in different solvent systems is shown ranging from 1.6×10^4 L mol^{-1} cm^{-1} to 2.1×10^3 L mol^{-1} cm^{-1}, which is corresponding to the HOMO–LUMO gap of 2.00–2.07 eV, which is theoretically within the visible light to near Infrared region.

3.1.4 The Computational Studies of N

The experimental data obtained were partially complemented by theoretical studies using DFT program at B3LYP/6-31G** level, to predict the optimized structure of **N** and its resultant complex **N-F** (Table 2). The optoelectronic properties of **N** and **N-F** complexed state were investigated by DFT calculations, in order to have a better insight in orbital behaviours, before and after binding with analytes. The HOMO of **N** was localized more on the naphthyl ancillary/anchoring ligand (Table 2), which translates into a smaller amplitude on the t_{2g} orbitals of the ruthenium metal. The LUMO of **N** are concentrated on the ruthenium metal center, extended over to the bipyridyl ring framework. The HOMO and LUMO levels are at − 10.57 eV and − 7.91 eV respectively, while their energy gap is 2.66 eV. The characteristics of the HOMO–LUMO energy gap (2.66 eV) exhibits the properties of dye sensitizers for solar cells, in which the absorption of a dye falls within the visible light region of the spectrum. The energy gap is in agreement with experimental data, where the energy gap range was found to be between 2.00 and 2.07 eV, which is well within the visible region, perhaps more to the solvent effect on the absorption of **N**. The theoretical HOMO–LUMO energy gap is relatively larger comparing to the experimental energy gaps (Table 1), because it was calculated in vacuum, instead of different solvents.

Furthermore, the characteristics of the absorption spectrum is also in agreement with the band gaps obtained, with the absorption maxima in the region of visible light which normally translates into 1.6–3.2 eV (800–400 nm). In addition, the complexed state of **N** with F$^-$ (**N-F**) was studied using DFT calculations as well, in order to understand the effect of binding on the optoelectronic properties

Table 2 The frontier orbitals of **N** and **N-F**

Compound	E_{HOMO}	E_{LUMO}	$E_{H\text{-}L}$
N-F	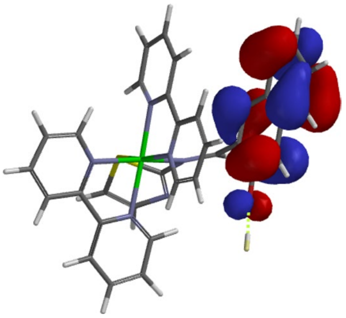 − 10.42 eV	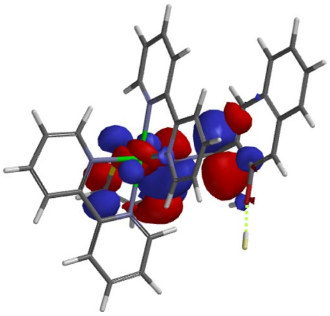 − 8.39 eV	2.03 eV

of **N**. Upon binding to F⁻, the electronic properties slightly changed in such a way that the HOMO levels changed to − 10.42 eV, which were still localized on the naphthyl ring system, while the LUMO level changed to − 8.39 eV, concentrated now more to the ruthenium metal only (Table 2). The HOMO–LUMO gap slightly decreased to 2.03 eV, which shows now a more favourable stable complex (**N-F**), comparing to **N**. The effect of hydrogen bonded F- to the structure is obviously influencing the optical and electronic properties, resulting into red shifted charge transfer band, as indicated by UV–Vis titrations between **N** and F⁻ (Fig. 5b).

Theoretically, the solvatochromic effect studies of **N** indicated that optical properties are influenced by solvent polarities. Evidently, the bad gap was found to be relatively smaller in vacuum (3.07 eV) as shown, comparing to when in solvents (Table 3). The contrast with experimental-derived values is consistent with the theoretical values, even though the two sets of bang gap (experimental vs theoretical) vary with a factor of 1 eV. In theory, ruthenium bipyridyl based complexes display the MLCT band in the visible region, in which in this case too, the two sets of band gap values correlate to absorption within the visible region. The band gap variances between the two sets (experimental vs theoretical) may be due to the ambiguity of the calculation method used, however, the values are still deemed to fall within the margin error. Inhere, the experimental values range from 2.0 to 2.07 eV, while for simulated values ranged from 3.37 to 3.42, (Table 3).

Furthermore, the transition states indicated that the MLCT in different solvents were all concentrated in the region of 400 nm (Table 4). Factually, the simulated transitions are conforming to some extend with the experimental results (Table 1). For instance, experimentally, **N** showed the highest molar absorptivity in acetone, and on the other hand simulated data similarly displayed the furthest and highest spectra in acetone, thus confirming the conformity of the two sets of data (experimental vs simulation). Therefore, the two sets of data are well in agreement with each other, confirming the photoresponse behavior of **N** in the visible region. Absorbing in the visible region is an indication of a potential solar cell material, as the dye is excited within the ideal solar functional range. The band gap values from the simulated values ranges within the 400–450 nm (3.35–3.81 eV) as displayed (Table 4), which is compatible to the experimental

Table 3 HOMO–LUMO energies and energy gaps of **N** in vacuum and different solvents optimized at B3LYP/6-31G**

	HOMO (a.u)	LUMO (a.u.)	H–L Gap (a.u.)	H–L Gap (eV)
Vacuum	− 0.389	− 0.276	0.113	3.07
Acetone	− 0.230	− 0.105	0.125	3.40
Methanol	− 0.227	− 0.102	0.125	3.40
Ethanol	− 0.229	− 0.104	0.125	3.40
DMSO	− 0.226	− 0.100	0.126	3.42
THF	− 0.245	− 0.121	0.124	3.37
Ethyl acetate	− 0.250	− 0.126	0.124	3.37

Table 4 Vertical excitation energies, MO contribution to major electronic transitions, oscillator strength and calculated H–L energy gaps of N due to the MLCT, computed in vacuum and in different solvents at the B3LYP/6-31G** level

	Excited state (Vis-region)	Excitation energies (nm)	Oscillator strength, f	MO contribution (Major contribution and composition)	H–L gap (eV)
Vacuum	4	445.50	0.1230	H –> L + 2 (73%)	3.35
	14	379.11	0.0548	H-2 –> L + 2 (73%)	3.92
Acetone	2	449.31	0.0812	H –> L (54%)	3.40
	8	403.06	0.0730	H-1 –> L + 2 (38%)	3.81
Methanol	2	448.83	0.0852	H –> L (55%)	3.40
	8	402.27	0.0727	H-1 –> L + 2 (37%)	3.78
Ethanol	2	449.14	0.0848	H –> L (54%)	3.40
	8	402.73	0.0737	H-1 –> L + 2 (38%)	3.81
DMSO	2	448.99	0.0976	H –> L (56%)	3.43
	8	402.01	0.0783	H-1 –> L + 2 (37%)	3.81
THF	3	445.79	0.0668	H –> L + 1 (46%)	3.51
	8	405.78	0.0678	H-1 –> L + 2 (47%)	3.81
Ethyl acetate	3	446.44	0.0733	H –> L + 1 (43%)	3.48
	8	406.50	0.0627	H-1 –> L + 2 (50%)	3.81

Table 5 HOMO–LUMO molecular orbitals of **N** in different solvents

	HOMO	LUMO
Vacuum	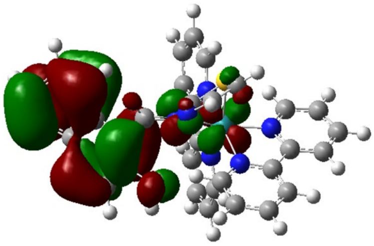 − 0.389 a.u	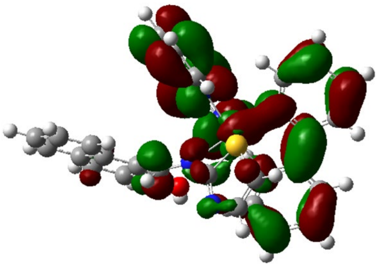 − 0.276 a.u
Acetone	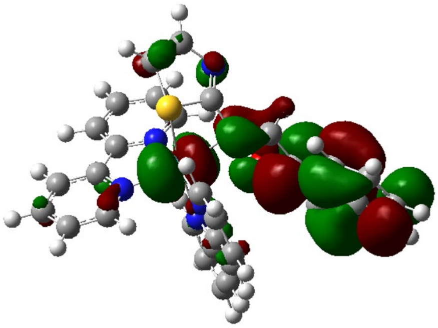 − 0.230 a.u	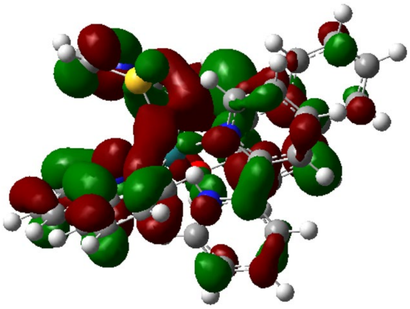 − 0.105 a.u
Methanol	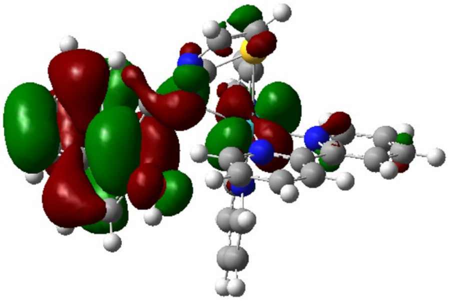 − 0.227 a.u	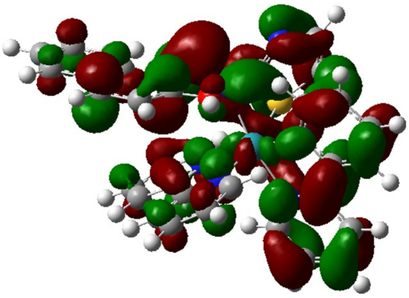 − 0.102 a.u
Ethanol	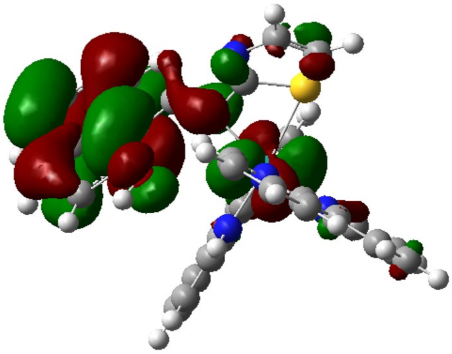 − 0.229 a.u	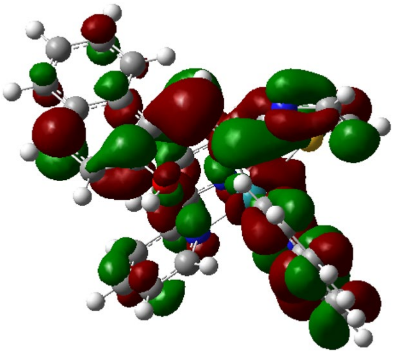 − 0.104 a.u

Table 5 (continued)

	HOMO	LUMO
DMSO	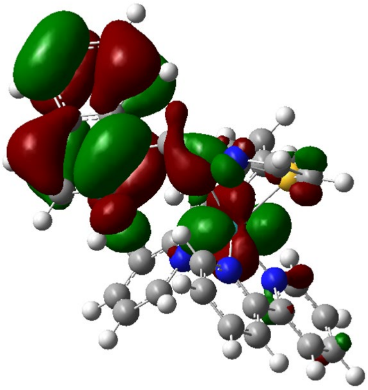 – 0.226 a.u	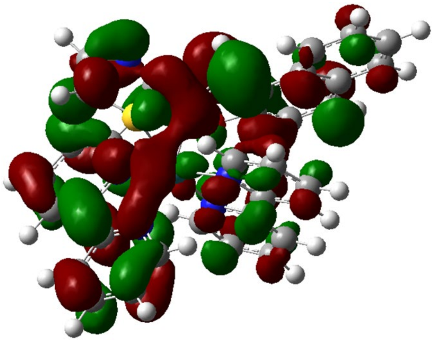 – 0.100 a.u
THF	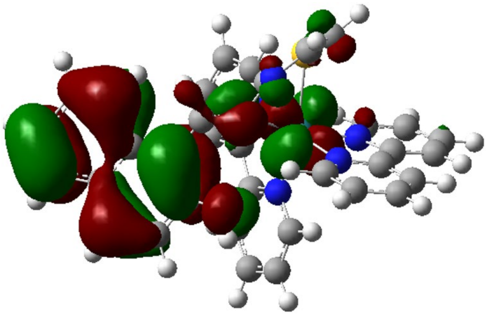 – 0.245 a.u	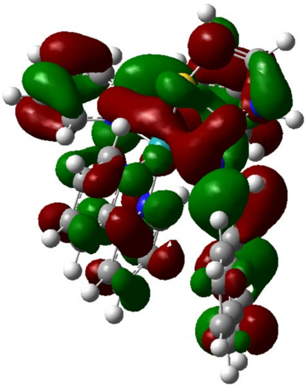 – 0.121 a.u
Ethylacetate	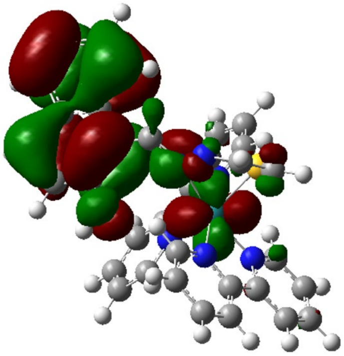 – 0.250 a.u	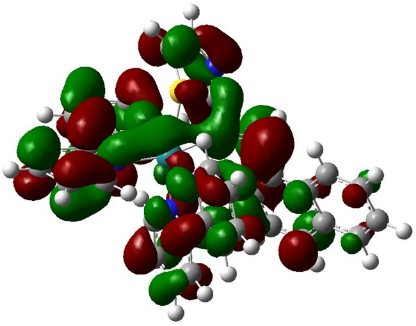 – 0.126 a.u

values (Table 1). In addition, it follows that the density of the HOMOs is concentrated more on the naphthyl group of the complex (Table 5), while the cloud of the LUMOs is situated on the bipyridyl groups, both in vacuum (reference) and all other solvents used.

3.1.5 UV–Vis Titration Spectra, the Redox Studies

The electronic interactions between ruthenium and the cerium ions were investigated using UV–vis oxidation titrations. Upon the molar equivalent addition of Ce^{4+}, the MLCT absorption band at 455 nm experienced a slight decreased in intensity while a new broad peak concomitantly appeared deep in the near-IR region of 700–900 nm (Fig. 4). The peak in the near-IR region is assigned to ligand to metal charge transfer (LMCT) of π-electrons of the ligand (bpy) to the oxidation state ruthenium (Ru^{3+}) transitions. Two distinctive isosbestic points at 461 nm and 588 nm are clearly visible which indicate the co-existence of two ruthenium oxidation states (mixed valence, Ru^{2+} and Ru^{3+}), showing the redox-based charge transfer activities from Ce^{4+} to Ru^{2+}., with one of the isosbestic points at 455 nm displayed and observed (Fig. 4 inset).

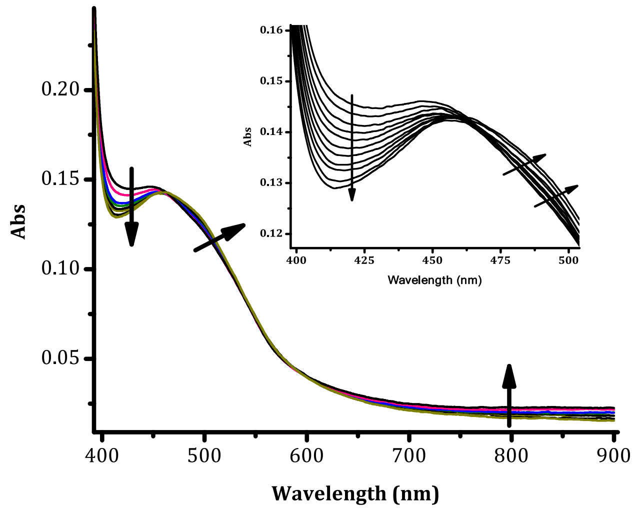

Fig. 4 UV–vis titration spectra of **N** (1.0×10^{-5} M) with $(NH_4)_2Ce(NO_3)_6$, 1–4 equiv., in ethanol

3.2 Chemosensing Property Studies of N

3.2.1 Anion Sensing Properties of N

The ruthenium complex-based sensor (**N**) is characterized by two high-energy distinctive peaks at 317 nm and 354 nm, as well as the low energy broader absorption band in the visible region (425–625 nm), observed in DMSO. The sequential molar addition of anions (CN^-, F^-, AcO^- and OH^-) as tetrabutyammonium (TBA) salts to **N** observed the disappearance of the band at 354 nm concomitant with the appearance of new bands at 414 nm and 425 nm (Fig. 5a–d), displaying a Stoke Shift of 60 nm. Additional to the spectral changes, the colour of **N** changed from orange to yellow (Fig. 6). In each case, an isosbestic point at 378 nm was observed, ascribed to the existence of two distinctive

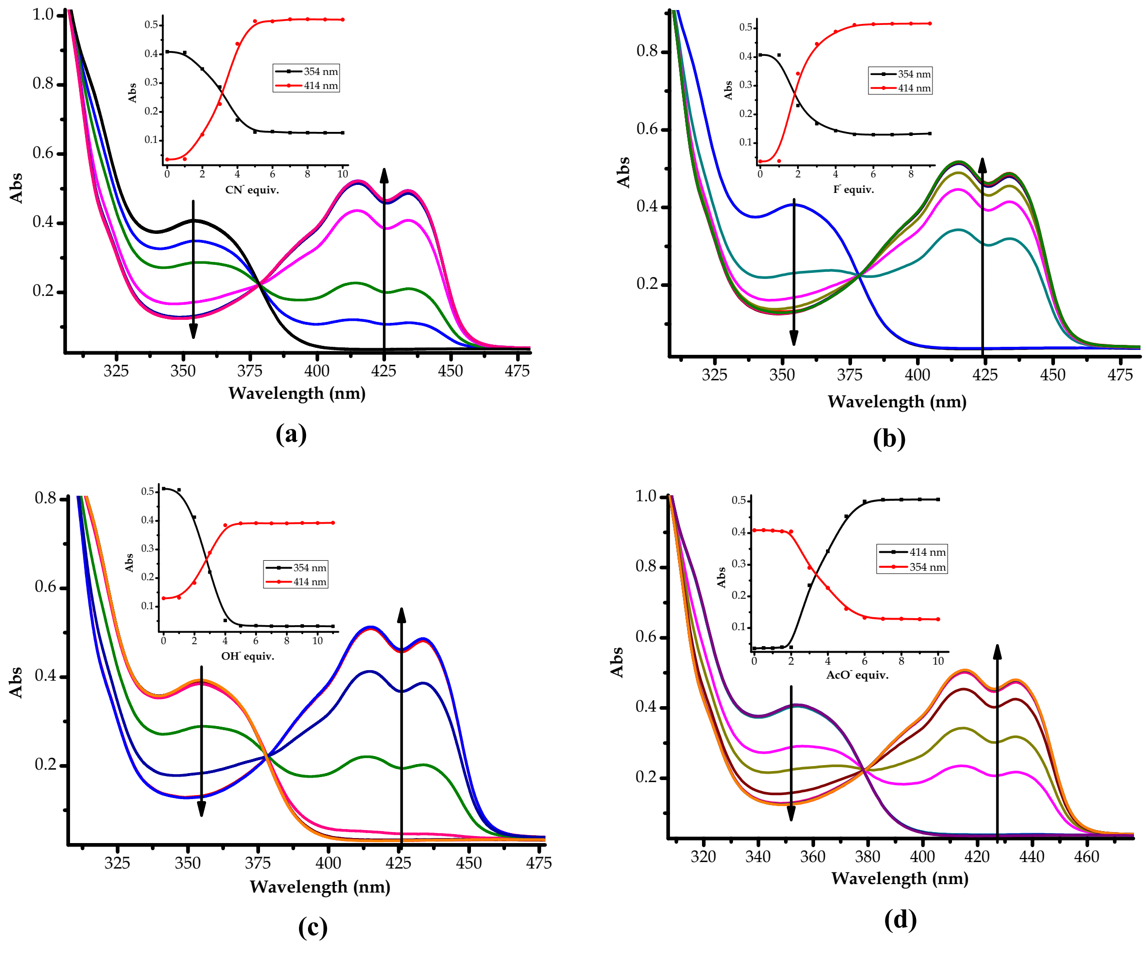

(a)

(b)

(c)

(d)

Fig. 5 Changes in UV/vis absorption spectra of **N** (1×10^{-5} M) upon the addition of 10 equiv. of **a** CN^-, **b** F^-, **c** OH^- and **d** AcO^- all in DMSO at 25 °C. The titration profiles of these anions are shown too (insets)

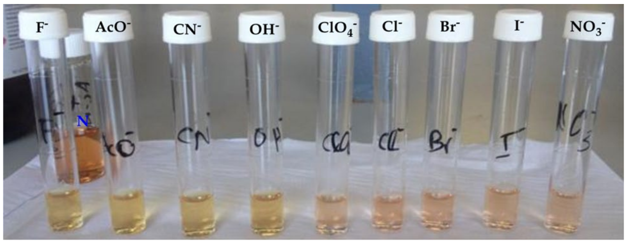

Fig. 6 Colorimetric activities observed upon the addition of different anions to **N** (1×10^{-5} M) in DMSO

species at equilibrium during the titration process. The colour changes are induced by the process of hydrogen-bonding between the host (**N**) and the guest (anion), which normally occurs upon an external stimuli is encountered by the molecule[41]. The titration profiles (Fig. 5a–d, insets) were observed displaying linearity behaviors, in each addition of anions to **N**.

Furthermore, the addition of other anions (Cl^-, Br^-, I^-, NO_3^- and ClO_4^-) did not induce any significant or noticeable changes (Fig. 6), which could be reflected by titration spectra of these anions (Fig. 7). Thus, there were no observable spectral changes induced upon the addition of other anions (Cl^-, Br^-, I^-, NO_3^- and ClO_4^-) as displayed in Fig. 7a, b. It follows that, the interaction of anions with **N** is expected to be via hydrogen bonding modes, between the N–OH and the more electronegative anionic species (CN^-, F^-, AcO^- and OH^-) coupled with their complimentary geometrical shapes and chemical footprints.

Generally, the interaction modes in chemosensing systems interact according to their electrophilicity and nucleophilicity potentials, based on the distribution sites of the LUMO in **N**. Firstly, the hydrogen bonding which involves the OH group where it serves as a convergent binding site of **N**, thereby interacting with the anions. The other process, is a deprotonation of the OH fragment, where an anion takes a proton from the OH receptor. Lastly, the other possible process is a nucleophilic addition, resulting in a bond formation reaction relied on the strong nucleophilicity of the anion. Given the high electronegative nature of F^- and AcO^-, these anions rightfully establish H-bond interactions, which leads to possibly deprotonation of **N**. However, the interaction via nucleophilic addition in which an anion would attack the C=N bond to give the addition product is likely to occur in the case of cyanide interaction. Furthermore, the detection of anions by **N** is likely to be a 1:1 ratio (Scheme 3), via the only OH group on the **N** molecular structure.

Evidently, the combined spectra of **N** with anions displayed vividly that CN^- was more strongly associated with the probe, based on its spectrum, which was higher than others (Fig. 7a). The strongly associated CN^- was followed by F^- and AcO^-, which are all associated with hydrogen-bonding which leads to deprotonation, especially when excess analytes are added. The less associated anion is OH^- with a spectrum lower than all other detected anions (CN^-, F^- and AcO^-) after the addition of 10 equiv. each to **N**, as displayed (Fig. 7a). The uniformity of spectra for all the anion is suggestive that the interaction mechanism between the host (**N**) and guests (CN^-, F^-, OH^- and AcO^-) was similar, ascribed to hydrogen-bonding, followed by deprotonation. In order to determine the limit of detection (LOD), absorption titration profiles were recorded after successive additions of 0.03 M of each anion (Figs. 5a–d, insets). The linear increases in absorption intensities were observed in the range from 0 to 6 µM, as shown in the absorption signal graphs (Fig. 8a–d), with R-squares ranging from 0.82731 (F^-), 0.87506 (OH^-), 0.91164 (CN^-) and 0.93513 (AcO^-) respectively. The limit of detection (LOD) was calculated to range between 10 and 20 nM using the 3α method [42].

LOD = 3 × Sd/m, where Sd is the standard deviation of the blank signal, and m is the slope of the calibration curve.

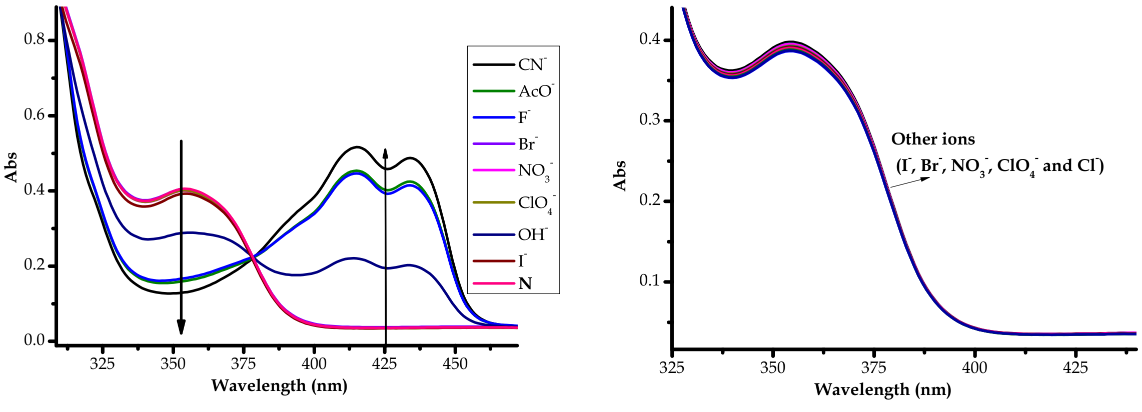

(a) **(b)**

Fig. 7 UV/Vis spectra of **N** (1.0×10^{-5} M) with various anions (10 equiv.) in DMSO, **a** where spectra of responsive (CN^-, AcO^-, F^-, OH^-) and **b** unresponsive anions (I^-, Br^-, NO_3^-, ClO_4^-) are displayed (insets)

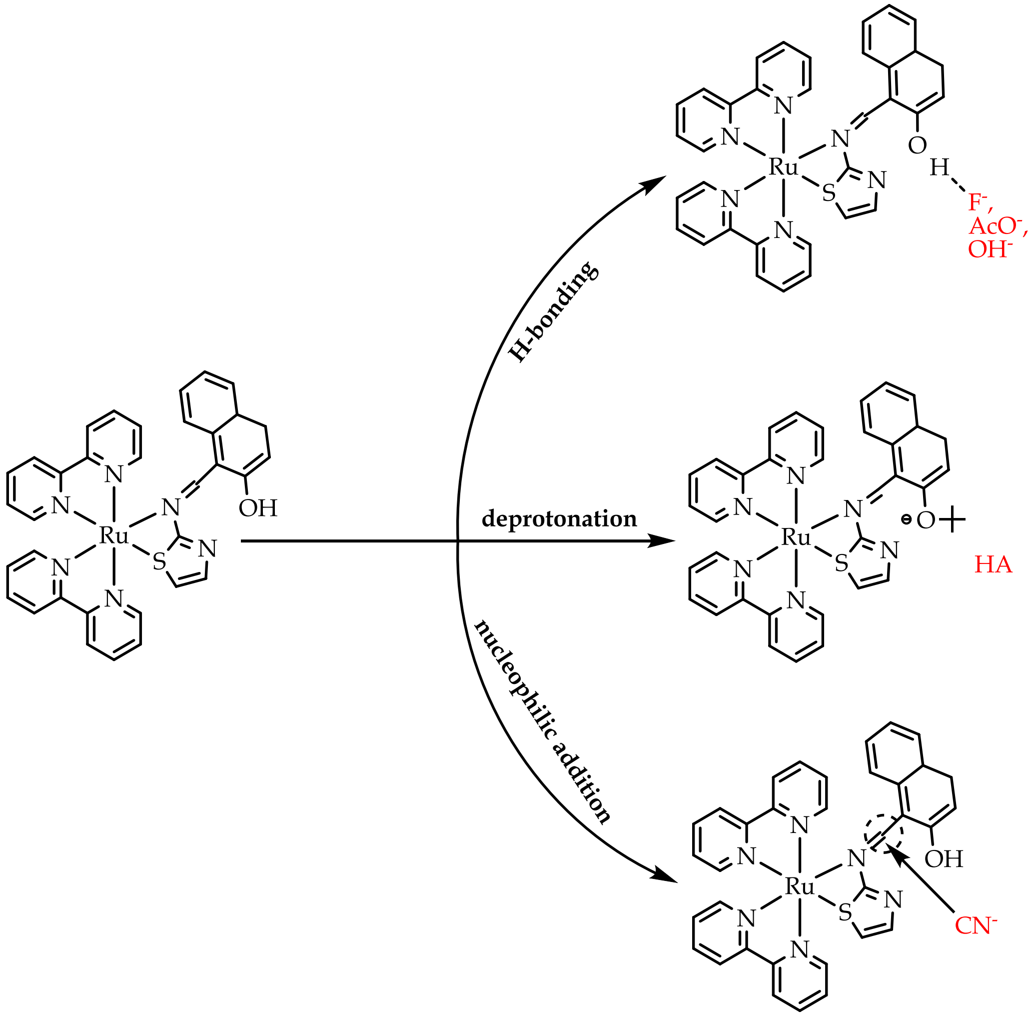

Scheme 3 The proposed interaction mechanisms of **N** with the anions

3.2.2 Fluorescence Studies of N Towards Anions

The fluorescence emission spectrum of **N** in DMSO was defined by a broad band with vibronic features, signifying that the emission was stemming from more than one excitation source in the structure (Fig. 9). The molar titrations of anions with **N** in DMSO was generally characterized by fluorescence emission enhancement, upon excited at 380 nm in DMSO. Generally, molecular structures containing an H-bond donor group associated with a basic site (O, N) usually undergo an ESIPT process. ESIPT is essentially a photo tautomerization in which an enol to keto transformation in the excited state occurs via an intramolecular hydrogen bond, involving the transfer of a hydroxyl proton to an electronegative atom. In this case, **N** was characterized by vibronic or dual emissions, ascribed to the enol and keto phototautomer forms (Scheme 4). Upon carrying out the fluorescence titrations, **N** displayed a weak emission band at 431 nm ascribed to the enol form and an intense emission band at 450 nm assigned to the keto form, when excited at 380 nm (Fig. 9). In addition, **N** displays remarkable Stoke shifts, with respect to the enol (431 nm) and keto (450 nm) forms. Noticeably, the Keto form emission resulted into a larger separation from the charge-transfer guided absorption band, with a Stoke shift of about 90 nm.

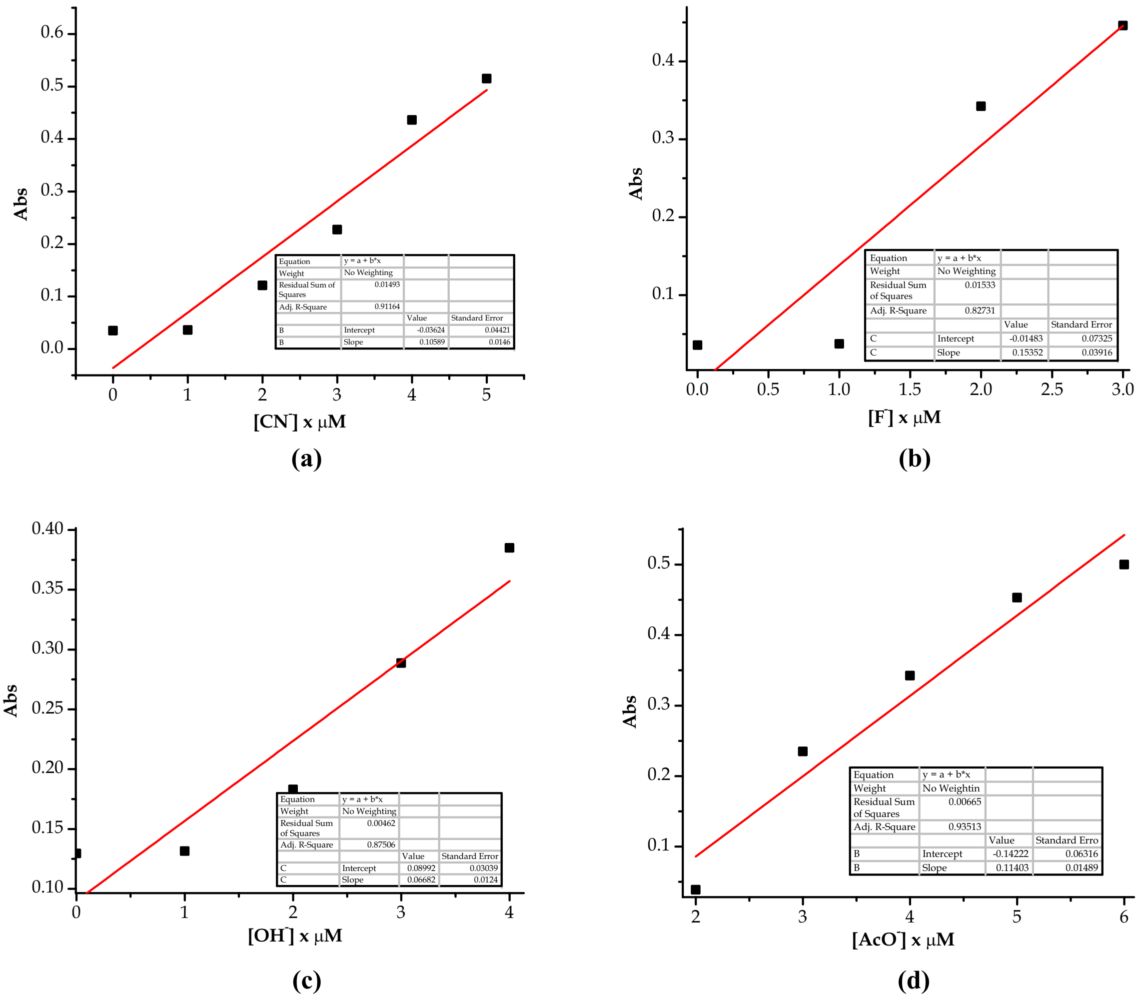

Fig. 8 Absorption signals of **N** with changing concentrations of **a** CN⁻ (0–5 μM) at 414 nm, **b** F⁻ (0–3 μM) at 414 nm, **c** OH⁻ (0–4 μM) at 414 nm, **d** AcO⁻ (0–6 μM) at 414 nm

Consequently, the molar addition of F⁻ to **N**, of up to 10 equiv., the vibronic emission bands were enhanced, resulting in the merging of the two bands to form one broader fluorescence spectrum front that increased by 6-folds (Fig. 9a). Thus, since there is an interaction between **N** and F⁻ it is assumed that the presence of -OH group is evident, which inhibits the enol-imine to keto-amine tautomerism which upon titration results in the slight blue-shifted emission of 10 nm. Notingly, the addition of similar equivalents (15–20 equiv.) of OH⁻ (Fig. 9b) and CN⁻ (Fig. 9c), the same effect of fluorescence enhancement was observed, characterized by slightly blue-shifted emissions, OH⁻ (10 nm) and CN⁻ (8 nm). The interactions with anions are enabled by the charge transfer driven hydrogen-bonding mechanism, which is reflected in both colorimetric, fluorometric and spectrometric observations. It appeared that the complex **N-F** formed was more emissive than the **N-CN** and **N–OH**, based on the fluorescence intensity displayed upon adding each of these anions (Fig. 9).

3.2.3 The FTIR Studies of N

The FTIR vibrational spectra for **N** and **1**, are characterized by two prominent vibrational bands in the regions of 1268–1567 cm^{-1} ascribed to the C=N stretching modes and 2865–3178 cm^{-1} assigned to the OH group stretching (Fig. 10a). The presence of the latter vibrational band (OH) confirms that the OH group is present in both the ligand (**1**) and the ruthenium complex (**N**), and this site is where the interaction activities with anions is taking place.

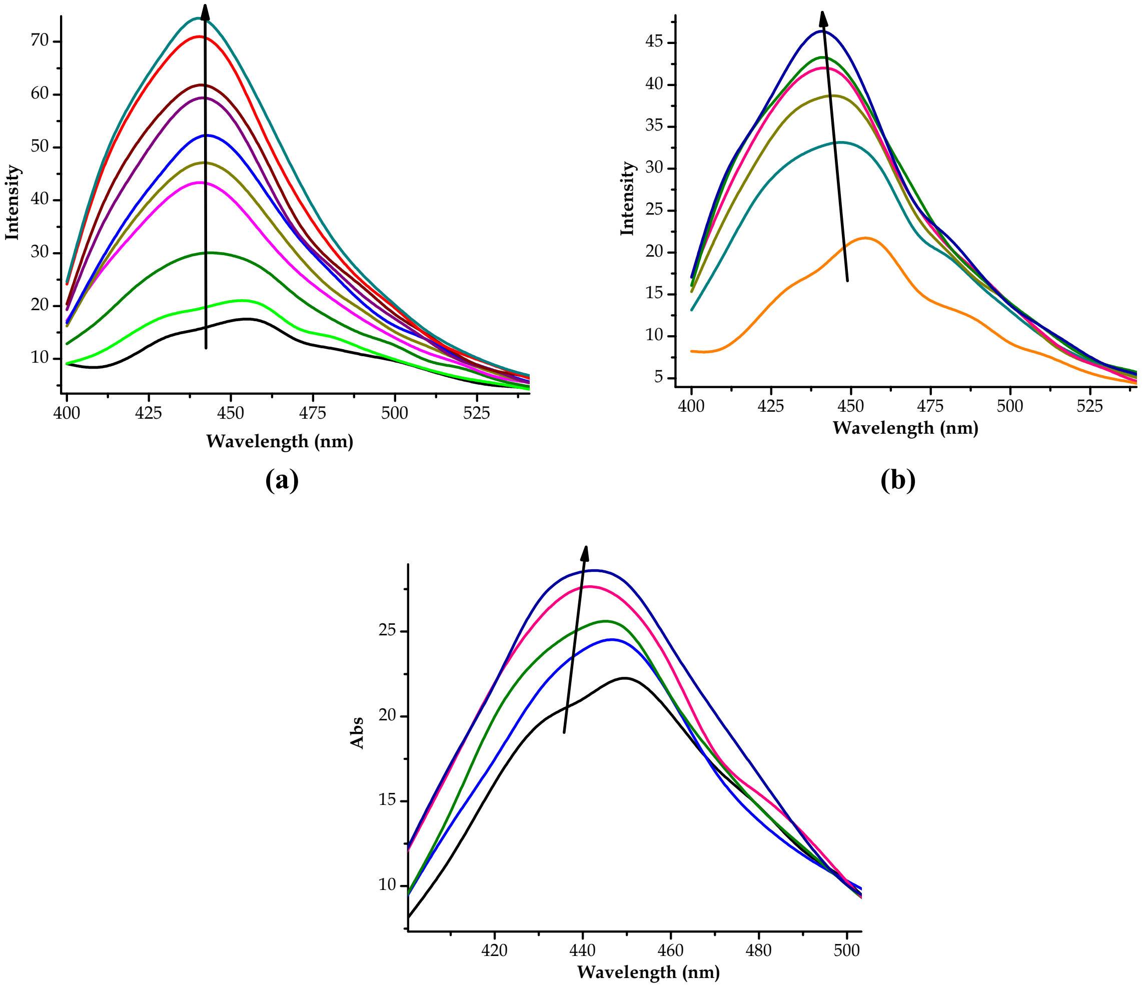

(a)

(b)

(c)

Fig. 9 Fluorescence titration spectra of **N** (1×10^{-5} M) with of **a** 10 equiv. F^-, **b** 12 equiv. OH^-, **c** 20 equiv. CN^- in DMSO

Since, the interaction between **N** and anions is predicted and proposed to occur via hydrogen bonding, it is evidently supported by FTIR titration results. The comparison of **N** and **N**-anion titrations spectra reveals the appearance of a new vibrational band at the 2284–2393 cm^{-1} region, concomitantly with the disappearance of the absorption band at the 2865–3178 cm^{-1}, upon the addition of any of the anion (Fig. 10b). Adding to that, multiple identical absorption bands in the 500–1750 cm^{-1} region associated mostly to the $Ru(bipy)_3$ structure are present in both **N** and **N**-anion titration spectra. The general predicated vibrational spectra for basic functional groups are tabulated below for comparison with obtained experimental and theoretical data (Table 6).

Notingly, the vibrational band at 2889–3036 cm^{-1} ascribed to the O–H functional group on **N** and **1** structures, interacts with CN^- via hydrogen bonding resulting in the deprotonation process. The band at 2284–2393 cm^{-1} also appears in the titration spectra of **N**-F, **N**–OH and **N**-AcO, which can be attributed to the structural rearrangement of the complex evolving from the destabilized HOMO, caused by the **N**-anion interaction at the OH group. The simulated IR spectra of **N** are principally in alignment with experimental results, such as 3811 cm^{-1} (O–H group), 3229 cm^{-1} (-CN group) and 1616–1770 cm^{-1} (aromatic bending), however, slightly red shifted on the simulated results (Fig. 10c). The disparity between experimental and theoretical spectra may stem from the presence of strong hydrogen-bonding

Scheme 4 The photophysical properties of **N** detailing the ESIPT process

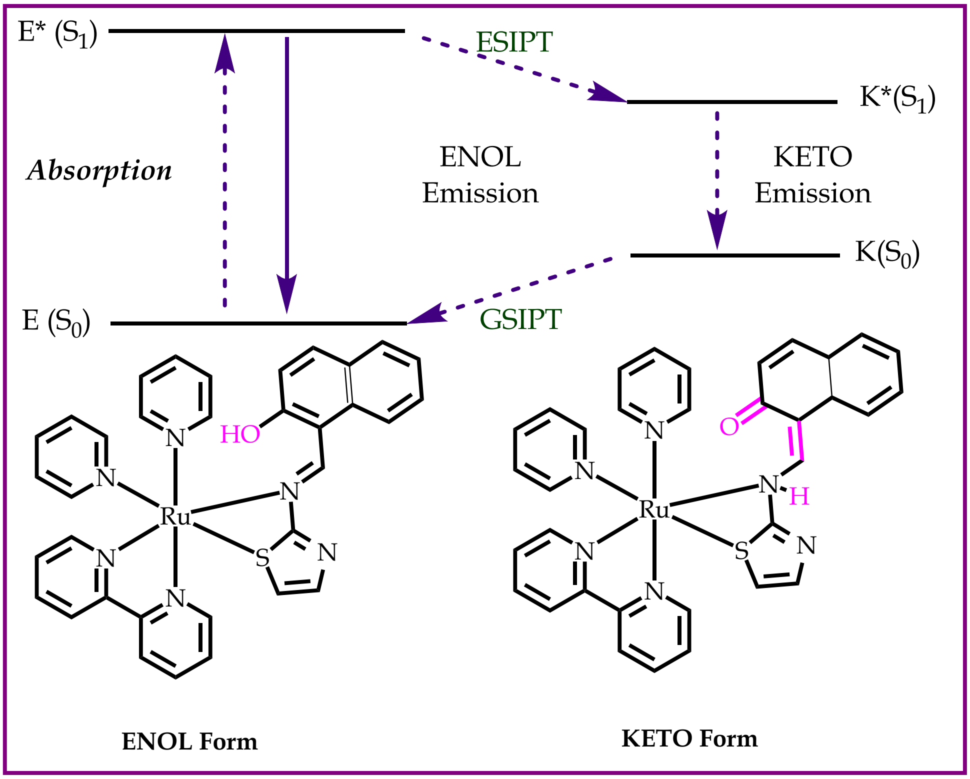

group in the structure (-OH group), which can simultaneously undergo tautomerism. The tautomeric effect, which enables the structure to interchangeably appear in a KETO and ENOL form, is highly likely to have influence in the experimental and theoretical spectra, thus causing slight vibrational spectra disparity as observed. Since theoretical simulation had focused on the ENOL form, it is highly probable that experimental data could exhibit the characteristics of both ENOL and KETO, resulting in the differences observed in the two sets of data. In addition, the effect of deprotonation of **N** was observed by the absence or rather the disappearance of the -OH group in the **N**-F spectra, usually leading to the formation of a hydrogen difluoride ion $[FHF]^-$ [43].

4 Conclusion

In summary, we have synthesized a dual functional molecular module based on the metal complex, with resonating charge transfer mechanisms (ESIPT) well matched for applications in molecular photovoltaics and chemosensing applications. The dye sensitizing properties were investigated through solvatochromism among other properties, and showed exquisite optoelectronic properties that are potential prerequisites to ideal dye sensitizer for solar cells, as supported by HOMO–LUMO gap calculations, thus **N** can be a potential DSSC. Additionally, the module has excellent chemosensing properties which can be exploited into real time applications to develop sensing kits. Comparatively, the sensor showed strong affinity towards CN^- among other competitive ions used. In addition, fluorescence properties have demonstrated that the presence of these anions have a positive emissive effect on the sensor, through fluorescence enhancement. Thus, **N** can be categorized as a dual functional molecular probe which exhibits basic characteristics for an ideal dye sensitizer, and a chemosensor, usually ease-to-prepare and apply, as well as stability in a range of conditions.

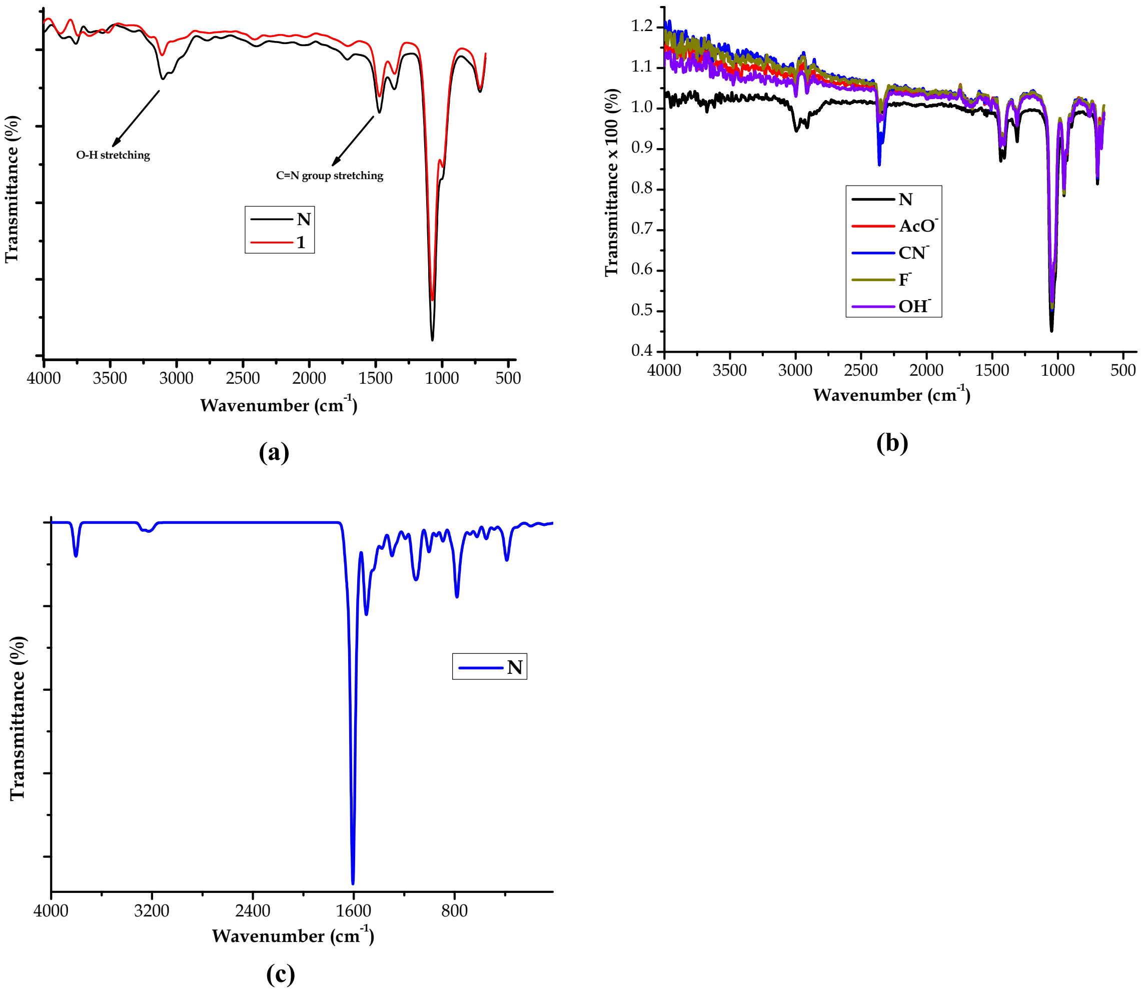

(a)

(b)

(c)

Fig. 10 FTIR spectra of **a** **N** & **1**, **b** **N** in the presence of anions shown, and **c** simulated spectra of **N**

Table 6 Summarised table of FT-IR titration vibrational bands of **N** with the selective anions

Wavenumber (cm^{-1})	Functional groups	Band description
500–1750	C–H (Alkane bending) C=C (Aromatic bending)	Multiple strong, weak and narrow bands
2284– 393	C≡N (Nitrile stretching) Structural rearrangement	Variable medium band emerging after every titration
2889–3036	O–H (Phenol or alcohol stretching)	Broad weak band disappearing after every titration

Acknowledgements This work was supported by ARTEE PROJECT Engineers, the Department of Chemistry and Biochemistry, University of Namibia, Namibia. This was also supported by the Royal Society-DFiD Africa Capacity Building Initiative Award.

Declarations

Conflict of Interest No conflicts of interest to declare, from all authors.

References

1. O'Regan B, Grätzel M (1991) A low-cost, high-efficiency solar cell based on dye-sensitized colloidal TiO2 films. Nature 353:737–740. https://doi.org/10.1038/353737a0
2. Ryan M (2009) Progress in ruthenium complexes for dye sensitised solar cells. Platin Met Rev 53:216–218. https://doi.org/10.1595/147106709X475315
3. Maitani MM, Zhan C, Mochizuki D, Suzuki E, Wada Y (2014) Influence of co-existing species on charge transfer in

dye-sensitized nanocrystalline oxide semiconductors in aqueous suspension for H2 evolution under visible light. Appl Catal B Environ 147:770–778. https://doi.org/10.1016/j.apcatb.2013.10.016

4. Zulkifili ANB, Kento T, Daiki M, Fujiki A (2015) The basic research on the dye-sensitized solar cells (DSSC). J Clean Energy Technol 3:382–387. https://doi.org/10.7763/JOCET.2015.V3.228
5. Freitag M, Boschloo G (2017) The revival of dye-sensitized solar cells. Curr Opin Electrochem 2:111–119. https://doi.org/10.1016/j.coelec.2017.03.011
6. Richhariya G, Kumar A, Tekasakul P, Gupta B (2017) Natural dyes for dye sensitized solar cell: a review. Renew Sustain Energy Rev 69:705–718. https://doi.org/10.1016/j.rser.2016.11.198
7. Namuangruk S, Fukuda R, Ehara M, Meeprasert J, Khanasa T, Morada S, Kaewin T, Jungsuttiwong S, Sudyoadsuk T, Promarak V (2012) D-D–π–A-type organic dyes for dye-sensitized solar cells with a potential for direct electron injection and a high extinction coefficient: synthesis, characterization, and theoretical investigation. J Phys Chem C 116:25653–25663. https://doi.org/10.1021/jp304489t
8. Zhang X, Veikko U, Mao J, Cai P, Peng T (2012) Visible-light-induced photocatalytic hydrogen production over binuclear Ru II-bipyridyl dye-sensitized TiO 2 without noble metal loading. Chem Eur J 18:12103–12111. https://doi.org/10.1002/chem.201200725
9. Gong J, Liang J, Sumathy K (2012) Review on dye-sensitized solar cells (DSSCs): fundamental concepts and novel materials. Renew Sustain Energy Rev 16:5848–5860. https://doi.org/10.1016/j.rser.2012.04.044
10. Erten-Ela S, Colak SG, Ocakoglu K (2013) The first application of water-soluble ruthenium phenanthroline complex for dye sensitized solar cells from aqueous solution using PEDOT:PSS counter electrode versus platinum counter electrode. Inorganica Chim Acta 405:252–257. https://doi.org/10.1016/j.ica.2013.06.010
11. Wang H, Zhang KQ (2013) Photonic crystal structures with tunable structure color as colorimetric sensors. Sensors (Switzerland) 13:4192–4213. https://doi.org/10.3390/s130404192
12. Xu Y, Qiang LS, Yang YL, Wei LG, Wang P, Fan RQ (2016) Enhanced performance of ruthenium dye-sensitized solar cell by employing an organic co-adsorbent of N, N'-bis((pyridin-2-yl)(methyl) methylene)-o-phenylenediamine. Chin Chem Lett 27:127–134. https://doi.org/10.1016/j.cclet.2015.06.010
13. Jin Z, Masuda H, Yamanaka N, Minami M, Nakamura T, Nishikitani Y (2009) Efficient electron transfer ruthenium sensitizers for dye-sensitized solar cells. J Phys Chem C 113:2618–2623. https://doi.org/10.1021/jp8083748
14. Kannan Balasingam S, Lee M, Gu Kang M, Jun Y (2013) Improvement of dye-sensitized solar cells toward the broader light harvesting of the solar spectrum. Chem Commun 49:1471–1487. https://doi.org/10.1039/c2cc37616d
15. Yu X, Lin H, Lin H (2008) A colorimetric anion receptor containing the cis-Ru(bipy)22+ group. Transit Met Chem 33:829–834. https://doi.org/10.1007/s11243-008-9118-3
16. Zhang Y, Liu Z, Yang K, Zhang Y, Xu Y, Li H, Wang C, Lu A, Sun S (2015) A ruthenium(II) complex as turn-on Cu(II) luminescent sensor based on oxidative cyclization mechanism and its application in vivo. Sci Rep 5:8172. https://doi.org/10.1038/srep08172
17. Na Kim H, Xiu Ren W, Seung Kim J, Yoon J (2012) Fluorescent and colorimetric sensors for detection of lead, cadmium, and mercury ions. Chem Soc Rev 41:3210–3244. https://doi.org/10.1039/c1cs15245a
18. Khattab TA, Fouda MMG, Rehan M, Okla MK, Alamri SA, Alaraidh IA, Al-ghamdi AA, Soufan WH, Abdelsalam EM, Allam AA (2020) Novel halochromic cellulose nanowhiskers from rice straw: visual detection of urea. Carbohydr Polym 231:115740. https://doi.org/10.1016/j.carbpol.2019.115740
19. Khattab TA, Aly SA, Klapötke TM (2018) Naked-eye facile colorimetric detection of alkylphenols using Fe(III)-impregnated silica-based strips. Chem Pap 72:1553–1559. https://doi.org/10.1007/s11696-018-0409-7
20. Zimmermann LM, Nicolini J, Marini VG, Machado VG (2015) Anionic chromogenic chemosensors highly selective for cyanide based on the interaction of phenyl boronic acid and solvatochromic dyes. Sens Actuators B 221:644–652. https://doi.org/10.1016/j.snb.2015.06.135
21. Zhang X, Yin J, Yoon J (2014) Recent advances in development of chiral fluorescent and colorimetric sensors. Chem Rev 114:4918–4959. https://doi.org/10.1021/cr400568b
22. Zheng X, Cheng W, Ji C, Zhang J, Yin M (2020) Detection of metal ions in biological systems: a review. Rev Anal Chem 39:231–246. https://doi.org/10.1515/revac-2020-0118
23. Carter KP, Young AM, Palmer AE (2014) Fluorescent sensors for measuring metal ions in living systems. Chem Rev 114:4564–4601. https://doi.org/10.1021/cr400546e
24. Liu B, Zhuang J, Wei G (2020) Recent advances in the design of colorimetric sensors for environmental monitoring. Environ Sci Nano 7:2195–2213. https://doi.org/10.1039/d0en00449a
25. Uahengo V, Zhang Y, Xiong B, Zhao P, Cai P, Rhyman L, Ramasami P, Hu K, Cheng G (2016) A fluoro-chromogenic sensor based on organic molecular framework for Cu^{2+} and F^{-} in aqueous soluble DMSO. J Fluoresc. https://doi.org/10.1007/s10895-016-1945-6
26. Yoon J, Kim SK, Singh NJ, Kim KS (2006) Imidazolium receptors for the recognition of anions. Chem Soc Rev 35:355–360. https://doi.org/10.1039/b513733k
27. Xu Z, Pan J, Spring DR, Cui J, Yoon J (2010) Ratiometric fluorescent and colorimetric sensors for Cu2+ based on 4,5-disubstituted-1,8-naphthalimide and sensing cyanide via Cu2+ displacement approach. Tetrahedron 66:1678–1683. https://doi.org/10.1016/j.tet.2010.01.008
28. Gunnlaugsson T, Glynn M, Tocci (née Hussey) GM, Kruger PE, Glynn FM (2006) Anion recognition and sensing in organic and aqueous media using luminescent and colorimetric sensors. Coord Chem Rev 250:3094–3117. https://doi.org/10.1016/j.ccr.2006.08.017
29. Liu YW, Xiu Kao M, Wu AT (2015) Discriminating detection between F- and CN- by naked eye from Schiff base sensor. Sens Actuators B 208:429–435. https://doi.org/10.1016/j.snb.2014.11.039
30. Yang F, Akhtaruzzaman M, Islam A, Jin T, El-Shafei A, Qin C, Han L, Alamry KA, Kosa SA, Hussein MA, Asiri AM, Yamamoto Y (2012) Structure-property relationship of naphthalene based donor-π-acceptor organic dyes for dye-sensitized solar cells: remarkable improvement of open-circuit photovoltage. J Mater Chem 22:22550–22557. https://doi.org/10.1039/c2jm34363k
31. Uahengo V, Hamukwaya E, Endjala P, Naimhwaka J (2020) A potential naphthyl-thiazole-based organic dye and a ditopic chromogenic probe for CN- and Fe3+ with molecular logic functions. New J Chem. https://doi.org/10.1039/D0NJ03806G
32. Peng X, Wu Y, Fan J, Tian M, Han K (2005) Colorimetric and ratiometric fluorescence sensing of fluoride: Tuning selectivity in proton transfer. J Org Chem 70:10524–10531. https://doi.org/10.1021/jo051766q
33. Yadav UN, Pant P, Sharma D, Sahoo SK, Shankarling GS (2014) Quinoline-based chemosensor for fluoride and acetate: a combined experimental and DFT study. Sens Actuators B 197:73–80. https://doi.org/10.1016/j.snb.2014.02.075
34. Khattab TA, Allam AA, Othman SI, Bin-Jumah M, Al-Harbi HM, Fouda MMG (2019) Synthesis, solvatochromic performance, ph sensing, dyeing ability, and antimicrobial activity

of novel hydrazone dyestuffs. J Chem. https://doi.org/10.1155/2019/7814179

35. Bishnoi S, Milton MD (2015) Tunable phenothiazine hydrazones as colour displaying, ratiometric and reversible pH sensors. Tetrahedron Lett 56:6633–6638. https://doi.org/10.1016/j.tetlet.2015.10.041
36. Nishikawa M, Nomoto K, Kume S, Nishihara H (2012) Reversible copper(II)/(I) electrochemical potential switching driven by visible light-induced coordinated ring rotation. J Am Chem Soc 134:10543–10553. https://doi.org/10.1021/ja3028873
37. Thangadurai TD, Lee CJ, Jeong SH, Yoon S, Seo YG, Lee Y-II (2013) A novel colorimetric and fluorescent sensor for fluoride and pyrophosphate based on fluorenone signaling units. Microchem J 106:27–33. https://doi.org/10.1016/j.microc.2012.04.012
38. Qiao YH, Lin H, Shao J, Lin HK (2009) A highly selective naked-eye colorimetric sensor for acetate ion based on 1,10-phenanthroline-2,9-dicarboxyaldehyde-di-(p-substitutedphenyl-hydrazone). Spectrochim Acta Part A 72:378–381. https://doi.org/10.1016/j.saa.2008.10.007
39. Uahengo V, Zhou N, Xiong B, Cai P, Hu K, Cheng G (2013) Synthesis and characterization of a new dinuclear platinum(II) alkynyl complex with a ferrocene bridge and its interaction with silver ion. J Organomet Chem. https://doi.org/10.1016/j.jorganchem.2013.02.009
40. Byabartta P (2008) Ruthenium(II) phenylazopyridinearylazoimidazoles: Synthesis, spectral studies and redox properties. Russ J Coord Chem Khimiya 34:220–224. https://doi.org/10.1007/s11173-008-3012-6
41. Khattab TA (2020) From chromic switchable hydrazones to smart materials. Mater Chem Phys 254:123456. https://doi.org/10.1016/j.matchemphys.2020.123456
42. Jeong Y, Won Y, Yeong J, Park K, Chang P, Kim C (2015) Spectrochimica acta part A : molecular and biomolecular spectroscopy dual-channel detection of Cu 2 + and F À with a simple Schiff-based colorimetric and fluorescent sensor. Spectrochim Acta Part A 136:1649–1657. https://doi.org/10.1016/j.saa.2014.10.060
43. Madhuprasad BMP, Jung HY, Losic D, Kurkuri MD (2016) Anion sensors as logic gates: a close encounter? Chem Eur J 22:6148–6178. https://doi.org/10.1002/chem.201504396